Shear Behavior of Variable-Depth Concrete Beams with Wound Fiber-Reinforced Polymer Shear Reinforcement

Yang, Yuanzhang; Orr, John; Spadea, Saverio

Published in:
Journal of Composites for Construction

DOI:
10.1061/(ASCE)CC.1943-5614.0000899

Publication date:
2018

Document Version
Peer reviewed version

Shear behavior of variable-depth concrete beams with Wound-Fiber-Reinforced Polymer shear reinforcement

Yuanzhang YANG[1*], John ORR[2], Saverio SPADEA[3]

[1]University of Bath, Department of Architectural and Civil Engineering,
BRE Centre for Innovative Construction Materials
Bath, BA2 7AY, UK

[2]University of Cambridge, Department of Engineering,
Cambridge, CB2 1PZ, UK

[3]University of Dundee, School of Science and Engineering,
Dundee, DD1 4HN, UK

[*] Corresponding author: y.yang3@bath.ac.uk

[2]: jjo33@cam.ac.uk

[3]: s.spadea@dundee.ac.uk

Author Accepted Manuscript version, final version available via
DOI 10.1061/(ASCE)CC.1943-5614.0000899

Abstract

A novel shear reinforcing system, Wound Fiber Reinforced Polymer (W-FRP), is proposed that capitalizes on the flexibility of carbon fiber to create durable reinforcement cages for geometrically optimized concrete structures, thereby unlocking new potential to minimize carbon emissions associated with new concrete structures. FRP shear design methods have been extensively validated against prismatic beam tests, but variations in geometry are not yet considered. This paper proposes revised design methods, validated against tests on eight W-FRP reinforced variable-depth concrete beams, to examine the contributing factors to shear capacity. It is shown that the corner strength, orientation, and compression concrete confinement provided by W-FRP links, along with the contribution to shear of longitudinal bars are key design parameters. Optimizing the W-FRP pattern is found to provide as much as 50% shear capacity enhancement. The variable-depth geometry tested in this paper use 19% less concrete than an equivalent strength prismatic beam. Both reinforcement and geometry optimizations are the key steps towards achieving minimal material use for concrete structures.

Keyword: Wound-Fiber-Reinforced Polymer (WFRP), variable-depth beams, Shear Design.

Introduction

Concrete is the most widely used artificial material in the world because of its low cost, versatility, ease of use, and wide availability (Barcelo*, et al.*, 2014). Production of Portland cement reached 4.2 gig tons (Gt) in 2016 (US Geological Survey, 2017) and its production now accounts for more than 5% of annual global carbon emissions (Boden*, et al.*, 2013, Flower and Sanjayan, 2007).

One route to reducing these carbon emissions is to build optimized concrete structures with minimal embodied energy. The optimization of structural geometries is achieved by providing everywhere the strength and stiffness required by an envelope of design actions. Research has shown that optimized beams can save as much as 40% of concrete when compared to prismatic beams with the same load capacity (Bailiss, 2006, Garbett*, et al.*, 2010).

However, achieving optimized geometries with conventional steel reinforcement can be problematic, as precise bending of longitudinal bars and the fabrication of variable height transverse bars adds both labor and time related costs. In addition, although steel is theoretically protected from corrosion by the alkaline environment inside concrete, about €5 billion is still spent on repairing reinforced concrete (RC) structures in western Europe as a result of corrosion related damage each year (Hartt*, et al.*, 2007, Markeset*, et al.*, 2006, Schmitt, 2009).

A durable alternative is found for concrete structures in the use of Fiber Reinforced Polymers (FRP). Although the material costs of glass- and carbon- FRP are currently higher than steel (Nystrom*, et al.*, 2003), their corrosion resistance can result in more durable structures with subsequently lower maintenance costs in service (Nishizaki*, et al.*, 2006, Shapira and Bank, 1997).

In this paper, the flexibility of carbon fiber filament is used to establish a new potential for the manufacture of reinforcement cages for optimized geometries (Spadea*, et al.*, 2017), Fig. 1. A filament winding process is used to produce Wound Fiber Reinforced Polymer (W-FRP) shear reinforcement. Carbon fiber tows are coated in resin and wet-wound around longitudinal CFRP bars. The resulting W-FRP cage is lightweight, easily transported, and easy to position in formwork before casting. This unlocks the potential for structural optimization of concrete, where complex internal reinforcement geometries are required. The resulting concrete structure is thus both materially efficient and durable.

Despite the potential for lightweight and flexible FRP materials to enable structural lightweighting and durability enhancements there has been little exploitation of this potential. Instead, FRP reinforcement is frequently shaped and used like steel, despite the two materials having fundamentally different properties and advantages. In addition, there is not yet a consistent design approach for such structures, particularly with respect to shear behavior.

This paper presents a new experimental study to address this by using W-FRP in beams with variable-depth geometries and examining the various contributing factors to shear resistance. New proposals for design with both codified methods (CSA S806 (2012) and ACI 440.1 (2015)) and the Modified Compression Field Theory (MCFT) model (Vecchio and Collins, 1986) are made based on the new requirements of variable-depth beams reinforced with W-FRP and validated against new structural test data.

W-FRP shear design

Existing methods

Shear design equations for FRP reinforced beams in existing codes adopt similar expressions to those used in steel RC beams, as shown in Eq. 1 (ACI 440.1 (2015)) and Eq. 3 (CSA S806 (2012)), where a summation of concrete (V_c) and shear reinforcement (V_f) contributions is made. The shear contribution of shear links in Eq. 1 and Eq. 3 are expressed with the shear reinforcement ratio (ρ_{fv}). In ACI 440.1 (2015), the influence of FRP longitudinal flexural reinforcement on V_c is considered by a factor k which is a function of reinforcement ratio ρ_f and modular ratio n_f (Eq. 2). A 45-degree truss model is adopted to describe the contribution of shear links (V_f). CSA S806 (2012) adopts various factors to consider the shear contribution of concrete including concrete density (λ), bending moment (k_m) and reinforcement rigidity (k_r) and a variable-angle truss model is adopted to consider the contribution to shear capacity from the transverse reinforcement.

Eq. 1

$$V_{ACI} = V_c + V_f = \frac{2}{5}\sqrt{f_c^{'}}\, b_w k d + \rho_{fv} f_{fv} b_w d$$

Eq. 2

$$k = \sqrt{2\rho_f n_f + (\rho_f n_f)^2} - \rho_f n_f$$

Eq. 3

$$V_{CSA} = V_c + V_f = 0.05\lambda\phi_c k_m k_r (f_c^{'})^{\frac{1}{3}} b_w d + 0.4\phi_F \rho_{fv} f_{fu} b_w d_v \cot\theta$$

In addition to codified equations, Modified Compression Field Theory (MCFT) (Vecchio and Collins, 1986) is considered as an effective design and analysis method for FRP

RC beams (El-Sayed and Soudki, 2010, Razaqpur and Spadea, 2014, Stratford and Burgoyne, 2003). MCFT was developed by studying RC panel elements under pure shear or shear and axial force. It considers the responses including stress equilibrium, strain compatibility, constitutive relations, and crack behavior (Bentz*, et al.*, 2006). Although simplifications to MCFT have been made for prismatic beams by Bentz*, et al.* (2006) and Hoult*, et al.* (2008), they are not used here as MCFT relates the behavior of cracked concrete to the average shear stress, which is influenced significantly by the geometry of a beam. The classical equations are adopted in full following the approach proposed by Vecchio and Collins (1986).

Whilst considerable validation of these methods exists for prismatic beams, relatively little work has been undertaken for variable-depth beams. In order to adapt the existing design methods to optimized W-FRP RC beams, it is necessary to consider the additional parameters of (i) inclined longitudinal flexural reinforcement, (ii) variable-depth geometries, (iii) the strength of W-FRP shear links at their corners (Spadea*, et al.*, 2017) and (iv) the inclination of W-FRP shear reinforcement to the beam axis.

Inclined longitudinal reinforcement

Where longitudinal tensile reinforcement is inclined, as is the case in variable-depth beams, a vertical component of force ($\boldsymbol{V_t}$) can be considered to resist shear as shown in Fig. 2. Taking a cut along an assumed concrete strut, the axial tensile force in longitudinal bars at the support is composed of two parts: a flexural tensile force ($\boldsymbol{T_f}$) and an additional tensile force caused by shear ($\boldsymbol{F_{td}}$). The flexural tensile force is calculated based on bending equilibrium of the cross section. The additional tensile force arises from equilibrium of the truss model. In CSA S806 (2012), the additional tensile force is specified as Eq. 4, where $\boldsymbol{V_{tf}}$ is vertical component of flexural tensile force in longitudinal bars. The resulting shear contribution of longitudinal bars is calculated using Eq. 5.

Eq. 4

$$F_{td} = 1.3(V_a - 0.5V_f - V_{tf})$$

Eq. 5

$$V_t = T_f \sin\alpha_t + F_{td} \sin\alpha_t$$

Variable-depth geometries

Considering elastic behavior in a statically determinate beam, the maximum shear stress on a cross section of a variable-depth beam is higher than is found in a prismatic beam of the same depth under the same loading, Fig. 3 (a) (Oden, 1967, Paglietti and Carta, 2009, Timoshenko, 1930). The shear stress distributions of the cracked variable-depth and prismatic reinforced concrete beams are shown in Fig. 3 (b) (Yang*, et al.*, 2015), where the difference between maximum shear stresses depends on the variable depth geometry and cross section location. The design case from Yang*, et al.* (2015) shows using the shear stress distribution in prismatic beams could result in over 30% underestimation of the maximum shear stress. It is concluded that the shear design for variable-depth RC beams based on the codes and standards assuming parabolic shear stress distribution of prismatic beams could be unconservative (Paglietti and Carta, 2009, Yang*, et al.*, 2015).

Transverse reinforcement corner strength

For FRP transverse reinforcement, localized stress concentrations and the intrinsic weakness of fibers perpendicular to their longitudinal axis are attributed to significantly reduced strengths at bends (Ahmed*, et al.*, 2009, El-Sayed*, et al.*, 2007, Lee*, et al.*, 2013). The tensile strength of FRP for shear design, f_{fv}, is limited in ACI 440.1 (2015) to the minimum value of (i) strength at an ultimate strain of 0.4% or (ii) strength at the bent portion of shear links given by Eq. 6. CSA S806 (2012) limits the ultimate strain in

any FRP shear reinforcement to 0.5%. In Eq.3, a shear strength reduction factor of 0.40 is incorporated to account for reduced shear reinforcement corner strength.

The rectangular cross section of W-FRP shear links, which arises from their manufacturing process, is beneficial and leads to higher corner strengths than a conventional circular cross section shear link of the same area as the distance between outer and inner radius at the corner is reduced (Spadea*, et al.*, 2017). Eq. 7 was proposed by Spadea*, et al.* (2017) to calculate the corner strength of W-FRP reinforcement.

Eq. 6

$$f_{fb} = (0.05 \cdot \frac{r_b}{d_b} + 0.3) f_{fu}$$

Eq. 7

$$f_{fb} = (0.03 \cdot \frac{r_b}{d_{fi}} + 0.35) f_{fu}$$

Inclined W-FRP shear reinforcement

Inclined transverse reinforcement can provide a more effective mechanism for resisting shear (BSI, 2004). In tests on W-FRP reinforced prismatic beams (Spadea*, et al.*, 2017), diagonal links were found to be more effective than vertical links. As the manufacturing process for W-FRP allows the designer to specify the inclination of each leg of the reinforcing cage, it is therefore feasible to choose the reinforcement geometry in an optimal way to achieve peak shear performance.

Proposed design method

Inclined longitudinal reinforcement

The shear capacity of a beam with inclined longitudinal bars is given by Eq. 8:

Eq. 8

$$V_u = V_c + V_f + V_t$$

The value of shear resistance provided by linear elastic longitudinal bars V_t, is directly related to the applied load (Fig. 2). An iterative procedure is therefore required to calculate V_u. With known values of V_c and V_f, V_u is calculated by assuming a value of applied load, calculating the force in the longitudinal bar caused by bending moment and applied shear force, and hence calculating V_t. If the resulting value of Eq. 8 is different from the shear demand on the section, the applied load is changed and V_t re-calculated until V_u is equal to the shear demand on the section.

Variable-depth geometries

The shear strength of a variable-depth beam varies along its length. It may be feasible to design a variable-depth beam such that each section has precisely the required shear capacity for an envelope of applied loads, by calculating Eq. 8 at each cross section. Practical limitations such as minimum longitudinal bar curvature may result in small geometrical deviations from the ideal geometry.

In the MCFT method, normally the average shear stress of the cross sections in shear span of a prismatic beam is used to calculate the shear strength. To consider the variable-depth geometry, the shear contribution of concrete (V_c) and W-FRP (V_f) of all cross sections is calculated following the distribution of cracked variable-depth beams (Fig. 3 (b)).

Transverse reinforcement corner strength

Building on the methods of ACI 440.1 (2015) and CSA S806 (2012), it is proposed that the strength of W-FRP reinforcement may be determined by the actual corner strength of stirrups as measured in standardized tests (Spadea*, et al.*, 2017). In the revised ACI method, f_{fv} is taken as minimum value of (i) strength at ultimate strain of 0.4%, (ii)

strength calculated following Eq. 6 and (iii) the actual corner strength. In the revised CSA method, following Razaqpur and Spadea (2014), f_{fv} is taken as minimum value of (i) $0.4f_{fu}$ of W-FRP, (ii) strength at ultimate strain of 0.5% and (iii) the actual corner strength. The shear contribution from W-FRP is therefore calculated using Eq. 3. Note that the strength reduction factor of 0.40 present in Eq. 3 is removed and is included instead in condition (i) above as a limit on f_{fu} to align this proposal with Razaqpur and Spadea (2014). In the revised MCFT model, the corner strength of the shear links will use the actual performance of W-FRP shear links from test data (Spadea*, et al.*, 2017).

Inclined W-FRP shear reinforcement

The W-FRP shear reinforcement introduced in this paper includes both vertical and inclined links and the shear contribution of shear reinforcement in Eq. 1 and Eq. 3 only applies to vertical shear links. To include the effect of inclined shear links the W-FRP shear reinforcement ratio (ρ_{fv}) in Eq. 1 and Eq. 3 is rewritten as Eq. 9, which is also adopted in the revised MCFT method to calculate the shear contribution of concrete and shear reinforcement.

Eq. 9

$$\rho_{fv} = \frac{A_{fv}}{b_w s}(1 + \sin\alpha + \cos\alpha)$$

Design procedure

Revised ACI 440 and CSA S806

For a set of input parameters including material properties, span, and loading envelope:

1. Calculate shear and bending demand along element based on applied loading;
2. Divide the beam into equally spaced transverse sections;

3. Calculate minimum section effective depths and required area of FRP reinforcement following codified flexural design methods;
4. Initially estimate the area of transverse FRP reinforcement required, and at each section, calculate V_c and V_f (Eq. 1 and Eq. 3) with the corner strength of shear reinforcement specified in section 0 and the shear reinforcement ratio given by Eq. 9, accounting for any inclination of the reinforcement to the longitudinal axis;
5. At each section calculate the value of V_t based on the inclination and the tensile force of bars following Eq. 5;
6. At each section calculate the value of V_u using Eq. 8
7. Where V_u is less than the required capacity from (1), iterate the section geometry, area of transverse reinforcement, and transverse reinforcement arrangement, through steps 4-6 until the member resistance is greater than or equal to the required shear and bending demand.
8. Output member geometry and reinforcement arrangement.

Revised MCFT

For a set of input parameters including material properties, span, and loading envelope:

1. Calculate shear and bending demand along element based on applied loading;
2. Divide the beam into equally spaced transverse sections;
3. Calculate minimum section effective depths and required area of FRP reinforcement following the flexural equilibriums of the sections;
4. Initially estimate the area of transverse FRP reinforcement required;
5. At each section, assuming an applied shear force V_a, calculate the strain of longitudinal bars and the shear contribution of longitudinal bars V_t with the flexural tensile force and additional tensile force (Eq. 4).

6. At each section, using the tensile strain of longitudinal bars, the shear resistance of concrete and shear links ($V_v = V_c + V_f$) is calculated as the integral of the shear stress distribution (Fig. 3 (b)) when the stress of the shear links across the shear crack reach their capacity at the corners (Eq. 7). The shear reinforcement ratio is given by Eq. 9, accounting for any inclination of the reinforcement to the longitudinal axis;
7. At each section calculate the value of V_u using Eq. 8
8. Where V_u is less than the required capacity from step 1, iterate the section geometry, area of transverse reinforcement, and transverse reinforcement arrangement, through steps 4-7 until the member resistance is greater than or equal to the required shear and bending demand.
9. Output member geometry and reinforcement arrangement.

Test program

Specimen design

To assess the proposed design methods and understand the shear performance of variable-depth beams reinforced with W-FRP, eight specimens were designed and tested in five groups with four shear reinforcement ratios (ρ_{fv}) and six shear reinforcement patterns (Fig. 4), Table 1. The specimens had the same web breadth (110 mm), length (1500 mm) and variable depth from 220mm at mid-span to 139mm at the supports. This geometry was determined by the limitations of curvature of the 1.5m length longitudinal bars.

Two control specimens were designed: Specimen T1 had no shear reinforcement and Specimen T4 was transversely over-reinforced to ensure flexural failure. The shear links in each specimen of group T2 and T3 were designed with constant spacing (vertical links) and variable angle (diagonal links). The different shear reinforcement

configurations were intentionally designed in order to result into the same shear reinforcement ratio, after the inclination had been considered. Group T5 was designed with different shear reinforcement ratios and the shear link in each specimen has a pattern of constant angle of 45° (diagonal links) and variable spacing (vertical links) along beam axis. All the designed shear reinforcement patterns shown in Fig. 4 were two legged and had a closed shape.

Material properties

All beams were designed with C25/30 concrete. Sixteen 100mm cubes were cast following BS EN 12390-1 (BSI, 2012) and tested in accordance with BS EN 12390-3 (BSI, 2009). The results are shown in Table 2 in which the mean cylinder strength is calculated as 80% of the cubic strength.

All shear links were manufactured using multiple layers of 50k Sigrafil carbon fiber tow (C T50-4.0/240-E100) with epoxy resin (Fyfe Tyfo S two component epoxy). Each layer of carbon fibre tow produces 4.28 mm^2 of CFRP reinforcement. All beams were reinforced longitudinally with 2 ø10 mm Aslan CFRP bars (Aslan 200 series). The corner strength of shear links different cross sections was adopted as the design strength of MCFT model and the tensile properties of the Aslan bars from the previous work of authors (Spadea, et al., 2017) were adopted as the design strength for all the three design methods, Table 3.

Specimen manufacture

To create the reinforcement geometries, a winding process was employed. The longitudinal bars were initially curved into the required geometry and held in position using a carbon fiber tendon, Fig. 5. The straight top bars and curved bottom bars were then assembled around a timber mandrel. Cable ties were attached to the longitudinal bars to mark the required W-FRP layout and prevent the W-FRP from sliding during the

winding process. Carbon fiber tows were impregnated with epoxy resin and wound around the cage in a continuous process to create each required reinforcement pattern (Fig. 5). Each cage was air cured for 72 hours.

The casting was conducted in steel formwork. Two foam wedges were placed in the formwork to create the variable-depth geometry of the specimen. Plastic spacers were used to maintain the required cover distance. After casting, all specimens were cured for 28 days prior to testing.

Test arrangement

The specimens were tested in three-point bending, Fig. 6. The test geometry was chosen to give a shear span to effective depth ratio of 2.5 to maximize the likelihood of shear failure (Kani, 1964) and to enable comparisons with previously reported prismatic beam tests (Spadea*, et al.*, 2017). One strain gauge was installed on the flexural bar at the loading point and each shear link in the shear span was strain gauged. Linear Variable Differential Transformers (LVDT) were installed at the loading point and mid-span to measure specimen displacement.

Test results

Load displacement curves for all specimens except T1, for which the LVDT failed during testing, are shown in Fig. 7. The test results are summarized in Table 4. Three types of failure modes were observed. Diagonal tension failure (DT) in specimens T1 and T2-1 (Fig. 8) was initiated by the major shear crack penetrating the web and, for specimen T2-1, shear reinforcement rupture at both the corners and straight part of the links. Shear compression failure (SC) in Specimens T2-2, T3-1, T3-2, T5-1 and T5-2 occurred with concrete crushing and the rupture of the shear reinforcement at its corners and straight part of the link (Fig. 9). Testing of Specimen T5-2 initially reached an applied load of 95kN at which point the hydraulic jack reached its maximum stroke.

Upon reapplication of the load, Specimen T5-2 failed in shear compression at 89kN. Debonding flexural failure (DF) in Specimen T4 was initiated by concrete crushing and pull-out of longitudinal bars as shown in Fig. 10.

All specimens exhibited similar stiffness during initial loading, Fig. 7. For specimens T2-2, T3-1, T5-1 and T5-2 failing in shear compression and specimen T4 failing in debonding, their stiffness was seen to decline after 80kN when concrete next to the loading point began to crush. This was also seen in specimen T3-2 but at the higher load of 100kN. After concrete crushing, displacement at the loading point for Specimens T2-2 and T5-1 increased by about 9.5% while maintaining a constant load. In specimen T3-2, after concrete crushing, the applied load increased by 10% with a 15% increase in deflection of loading point.

Table 5 shows the strains recorded in the longitudinal bars and resulting tensile force before the gauges were lost, and are plotted against the applied load in Fig. 11. Table 6 shows the average strains recorded in shear links crossing the main shear crack at the failure load.

Analysis and discussion

Shear reinforcement ratio

For specimens failing in shear compression or diagonal tension, as the reinforcement ratio increased so too did their ultimate capacity. Excluding the influence of the shear reinforcement pattern, it is seen from Table 4 that the capacities of T1 ($\boldsymbol{\rho_{fv}}$= 0), T2-1 ($\boldsymbol{\rho_{fv}}$= 0.25%) and T4 ($\boldsymbol{\rho_{fv}}$= 0.75%) increased with the shear reinforcement ratios. The higher shear capacity of T4 was ensured by the higher shear contribution of shear reinforcement and higher shear contribution of longitudinal bars, as a result of larger bar force. As shown in Table 5, with increasing shear reinforcement ratio, the tensile force in longitudinal bars of T4 was higher than T2-1 and T1, resulting in larger shear

contribution from longitudinal bars due to the relationship between applied load and bar force. However, the comparison between T2-1 ($\boldsymbol{\rho_{fv}}$= 0.25%) and T2-2 ($\boldsymbol{\rho_{fv}}$= 0.25%) demonstrate that the shear reinforcement ratio is not the only factor influenced the shear capacities of the specimens.

Shear reinforcement pattern

As expected in the proposed design methods, the shear capacities of the specimens were influenced by the corner strength of shear links and shear contribution of longitudinal bars reflected as the influence of shear reinforcement patterns. In addition, the patterns influence performance in another two aspects: (i) orientations of adjacent shear links and (ii) confinement of concrete.

For specimens with the same shear reinforcement ratio, denser patterns (i.e. more distributed links with smaller cross section area) resulted in higher shear capacities (Table 4). The ultimate capacity of T2-2 (92.6kN) was 50% higher than T2-1 (61.9kN) and the ultimate capacity of T3-2 (110.9kN) was 17% higher than T3-1 (94.9kN). The reason for the better performance of the denser pattern could be the higher corner strength of shear links with smaller cross sections (Table 3). The test data shows that shear links in specimens T2-2 and T3-2 had larger strains than in T2-1 and T3-1 respectively at their failure load, as shown in Fig. 12.

Improving the arrangement of the shear links led to a higher specimen shear capacity, which was caused by the higher shear contribution of shear links and the resulting higher longitudinal bar force. T2-2 exhibited higher bar force than T2-1 (Table 5), hence larger shear contribution of flexural reinforcement at a higher ultimate capacity. The other specimens cannot be compared as the strain gauges were damaged before the failure load.

The shear reinforcement pattern also can influence the load distribution in shear links and flexural reinforcement. The W-FRP patterns used in T5-1 and T5-2 led to higher tensile force in longitudinal bars as shown in Table 5. With longitudinal bars carrying more applied shear force, the shear links of T5-1 and T5-2 failed at lower average strains than specimens T2-2 and T3-2, even though the shear links in these four specimens are all made of one layer of 50K carbon fibers.

The denser patterns also attributed to smaller difference in orientations between adjacent vertical and inclined links (Fig. 12). Unlike steel shear links, which can theoretically reach their yielding point before shear failure no matter how they are arranged, FRP shear links will always have different strain values and some links may not be fully utilized before shear failure. During the tests, the rupturing of one critical shear link could led to the rupturing of the adjacent shear links with much lower strains. The denser patterns created similar strains between adjacent links and therefore more shear links can be utilized efficiently. This is justified by the higher capacities of specimens with smaller strain difference between vertical and inclined shear links. As shown in Table 6 and Fig. 12, the strain differences between diagonal links and vertical links of T2-2 and T3-2 were 1% and 3%, whereas in T2-1 and T3-1 the strain differences were 11% and 37%.

The denser patterns also provide additional confinement to the concrete in the compression zone. The improved confinement of concrete helped Specimen T3-2 to achieve a higher load of concrete crushing (approximately 20kN higher than the other specimens, with the same concrete) and hence resulted in the largest ultimate capacity.

Geometry

The specimens tested in this paper were not full-scale beams. The short length of the flexural reinforcement limited the curvature that could be achieved. The geometry of

the beams was determined as a result of compromise between optimization and ease of fabrication. Despite this, the specimens still consumed 19% less concrete than an equivalent strength prismatic beam. Comparisons between specimens tested in this paper and previous experimental research on prismatic beams (Spadea*, et al.*, 2017), which had the same width, clear span, and shear span/depth ratio but higher concrete strength and slightly higher shear reinforcement ratios, are shown in Table 7 and Fig. 13.

Only one specimen (T2-1) had a lower capacity than the similar prismatic beam, a difference that is attributed to the reinforcement pattern of T2-1. The remaining specimens exhibit higher ability to resist the applied shear force (V_a) while using less transverse reinforcement. In realistically sized beams, the longitudinal bars could be bent more conveniently and greater savings in concrete may be possible.

Predictions and test results comparison

The test results are compared to the predictions of ultimate capacity using the proposed revised codified methods (P^*_{ACI} and P^*_{CSA}), the direct application of Eq. 1 (P_{ACI}) and Eq. 3 (P_{CSA}) and the revised MCFT model (P_{MCFT}) in Table 8. All partial safety factors are set to 1.00 in these comparisons.

When the contribution of longitudinal bars to shear is not considered, the predictions of existing design codes, P_{ACI} (Eq. 1) and P_{CSA} (Eq. 3), were extremely conservative, with $P_{exp.}/P_{ACI}$ reaching 2.38 and $P_{exp.}/P_{CSA}$ reaching 1.49 on average. The conservative predictions are caused by the specified design strength of shear reinforcement. For ACI 440.1 (2015), the predicted capacities are governed by the 0.4% strain limit, Eq. 6. For CSA S806 (2012) (Eq. 3), the ultimate tensile strain limit in the straight part of shear reinforcement (0.5%) governs the predictions. More importantly, the shear contributions of inclined longitudinal reinforcement are not incorporated.

By considering the contribution of longitudinal bars, the predictions in the proposed revision to ACI 440.1, P^*_{ACI}, are conservative ($P_{exp.}/P^*_{ACI}$=1.45) and have a standard deviation of 0.25. With the variable truss angle model and higher design strength of shear reinforcement, the proposed revision to CSA S806, P^*_{CSA}, gives unconservative predictions ($P_{exp.}/P^*_{CSA}$= 0.89) and smaller standard deviation (0.13). In the proposed revisions, the 0.4% and 0.5% strain limit govern the predictions of ACI 440 and CSA S806 respectively. Therefore, although the actual corner strengths of W-FRP are considered together with specified strengths of shear reinforcement in the codes, the different corner strengths from various W-FRP patterns cannot be recognized.

However, for the transversely reinforced specimens, the revised MCFT model, P^*_{MCFT} has the best average predictions ($P_{exp.}/P_{MCFT}$= 1.11) with a standard deviation of 0.31. The revised MCFT model allows a differentiation between beams with the same reinforcement ratio but different reinforcement patterns. The capacity predictions vary between such specimens – for example T2 and T3 (Table 8) - and arise due to the different corner strengths of shear links with different cross-sectional areas.This advantage allows designers to optimize the W-FRP patterns with higher corner strength to achieve higher shear capacity or to save FRP material.

The predictions made for Specimen T4 cannot be calibrated because the unexpected premature debonding failure occurred and the real flexural and shear capacity of T4 was not obtained. The anchorage strength is also important in the design of variable-depth beams and is the topic of additional research beyond the scope of this paper.

The revised MCFT model results in two further unconservative predictions (T3-2 and T51). The predictions are reliant on the corner strength from tests of single W-FRP shear links, Table 3, (Spadea, et al., 2017). This is however not fully representative of the actual performance of multiple W-FRP shear links in a concrete specimen. The

different shear reinforcement patterns enabled the different average performance of multiple shear links (Table 6) and with limited research data, there is no empirical method to describe their influence to date.

Further work is required to relate tests on a single link to the capacity of multiple links within a structural member. The validity of the proposed design methods could be potentially improved by the actual corner strength of shear links with strength reduction factors of different shear reinforcement patterns based on further experimental research on W-FRP reinforced concrete.

Conclusions

The shear behavior of variable-depth beam reinforced with novel Wound-FRP reinforcement was explored. Attempts to design W-FRP reinforced concrete beams with optimized geometries were conducted and the validity of proposed new shear design methods was examined. With the test results and analysis, this research support the following conclusions:

1. As expected in the proposed shear design methods, corner strength of shear links and shear contribution of inclined longitudinal bars influence the shear performance. Shear reinforcement patterns with smaller differences in orientations between adjacent links give improved shear performance by reducing the strain differences between links, and providing improved concrete confinement.
2. With the beneficial effects of optimal shear reinforcement patterns, the shear capacities of specimens are enhanced which is highlighted by (i) the 50% higher shear capacity of T2-2 compared T2-1 and (ii) the 17% higher shear capacity of T3-2 compared with T3-1.

3. W-FRP overcomes the difficulty of reinforcing structures with complex geometries and thus enables reductions in material use through optimization. In this paper, 19% concrete savings are achieved compared to equivalent strength prismatic beams, despite geometrical limitations of the short bars used.
4. Direct application of existing code equations leads to extremely conservative predictions, most of which are less than 50% of the test results. By considering the shear contribution of longitudinal bars and the actual corner strength of shear links in different patterns, the predictions of revised MCFT model ($P_{exp.}/P_{MCFT}$= 1.11, SD = 0.31) have the best conservative correlations.
5. Adopting the actual corner strength of single shear link tests leads to two unconservative predictions in the revised MCFT model. Further research is required to establish a relationship between bend strength tests on a single W-FRP link and the performance of multiple W-FRP shear links in concrete and provide the basis for further revisions of proposed design methods.

Acknowledgements

The authors acknowledge and are grateful for the support of the BRE CICM (www.bath.ac.uk/bre), the University of Bath, EPSRC and China Scholarship Council who collectively fund the PhD position that has resulted in this work.

Data access statement

All data created during this research are openly available from the University of Bath data archive https://doi.org/10.15125/BATH-00455.

Notation

The following symbols are used in this paper:

A_{fv}	Cross section area of shear links (mm^2)
b_w	Width of the web of T beams (mm)
C	The compression force of concrete strut (kN)
d	Effective depth of beams (mm)
d_b	Diameter of bent shear reinforcement bars (mm)
d_{fi}	Depth of bent FRP shear links with rectangular cross section (mm)
d_m	Effective depth of beams at mid-span (mm)
k	Parameter to consider FRP reinforcement in concrete
k_m	Coefficient for the effect of moment at section on shear strength
k_r	Coefficient for the effect of reinforcement rigidity on shear strength
$f_c^{'}$	Specified cylinder compressive strength of concrete (MPa)
$f_{cm,cube}$	Average cubic strength of concrete (MPa)
f_{cm}	Cylinder strength of concrete calculated from test data (MPa)
F_{td}	Additional tensile force (kN)
f_{fb}	Strength of shear reinforcement at corners (MPa)
f_{fv}	Design strength of shear reinforcement (MPa)
f_{fu}	Tensile strength of FRP reinforcement (MPa)
n_f	Modular ratio between FRP and concrete
P	Applied load (kN)
$P_{exp.}$	Ultimate capacities of test specimens (kN)
r_b	Radius at the bent corners of shear reinforcement (mm)
Q_c	Quantity of concrete (m^3)
T	Tensile force of longitudinal bars (kN)
T_f	Flexural tensile force of longitudinal bars (kN)
P_{ACI}	Prediction of ultimate capacity using ACI 440 (kN)

P^*_{ACI}	Prediction of ultimate capacity using revised ACI 440 (kN)
P_{CSA}	Prediction of ultimate capacity using CSA S806 (kN)
P^*_{CSA}	Prediction of ultimate capacity using revised CSA S806 (kN)
P_{MCFT}	Prediction of ultimate capacity using revised MCFT model (kN)
$V_{exp.}$	Ultimate shear force carried by test specimens (kN)
V_f	Shear contribution of shear reinforcement (kN)
V_t	Shear contribution of longitudinal bars (kN)
V_{tf}	Vertical component of flexural tensile force, $T_f \sin \alpha_t$ (kN)
V_u	Shear capacity of beams (kN)
V_v	Shear contribution of shear links and concrete (kN)
α	Angle of diagonal shear links to the horizontal axis (º)
α_t	Angle of longitudinal bars to the horizontal axis (º)
ε_f	Strain of longitudinal bars
ε_{fv}	Strain of shear links
θ	Angle of concrete strut (º)
ρ_f	Flexural reinforcement ratio
ρ_{fv}	Shear reinforcement ratio
τ_{max}	Maximum shear stress (MPa)
ϕ_c	Resistance factor for concrete in CSA S806
ϕ_F	Resistance factor for FRP reinforcement in CSA S806
λ	Factor to account for concrete density in CSA S806

References

ACI (American Concrete Institute) (2015). "Guide for the Design and Construction of Concrete Reinforced with FRP Bars." *ACI 440.1 R-15*, Detroit, Michigan.

Ahmed, E., El-Sayed, A., El-Salakawy, E., and Benmokrane, B. (2009). "Bend Strength of FRP Stirrups: Comparison and Evaluation of Testing Methods." *Journal of Composites for Construction*, 14(1), 3-10.

Bailiss, J. (2006). "Fabric-formed concrete beams: Design and analysis." MEng, University of Bath, Bath.

Barcelo, L., Kline, J., Walenta, G., and Gartner, E. (2014). "Cement and carbon emissions." *Mater. Struct.*, 47(6), 1055-1065.

Bentz, E. C., Vecchio, F., and Collins, M. (2006). "Simplified modified compression field theory for calculating shear strength of reinforced concrete elements." *ACI Struct. J.*, 103(4), 614-624.

Boden, T., Marland, G., and Andres, R. (2013). "Global, Regional, and National Fossil-Fuel CO2 Emissions." Carbon Dioxide Information Analysis Center, Oak Ridge National Laboratory.

BSI (British Standards Institution) (2004). "Design of Concrete Structures: Part 1-1: General Rules and Rules for Buildings." *BS EN 1992-1-1:Eurocode 2*, London.

BSI (British Standards Institute) (2012). "Testing hardened concrete Shape, dimensions and other requirements for specimens and moulds." *BS EN 12390-1*, London.

BSI (British Standards Institute) (2009). "Testing hardened concrete: Compressive strength of test specimens." *BS EN 12390-3*, London.

CSA (Canadian Standards Association) (2012). "Design and construction of building structures with fibre-reinforced polymers." *CSA S806-12*, Ontario, Canada.

El-Sayed, A. K., El-Salakawy, E., and Benmokrane, B. (2007). "Mechanical and structural characterization of new carbon FRP stirrups for concrete members." *Journal of Composites for Construction*, 11(4), 352-362.

El-Sayed, A. K., and Soudki, K. (2010). "Evaluation of shear design equations of concrete beams with FRP reinforcement." *Journal of composites for construction*, 15(1), 9-20.

Flower, D. J. M., and Sanjayan, J. G. (2007). "Green house gas emissions due to concrete manufacture." *The International Journal of Life Cycle Assessment*, 12(5), 282-288.

Garbett, J., Darby, A., and Ibell, T. J. (2010). "Technical Papers: Optimised Beam Design Using Innovative Fabric-Formed Concrete." *Advances in Structural Engineering*, 13(5), 849-860.

Hartt, W. H., Powers, R. G., Lysogorski, D. K., Liroux, V., and Virmani, Y. P. (2007). "Corrosion Resistant Alloys for Reinforced Concrete."Geogetown.

Hoult, N., Sherwood, E., Bentz, E. C., and Collins, M. P. (2008). "Does the use of FRP reinforcement change the one-way shear behavior of reinforced concrete slabs?" *Journal of Composites for Construction*, 12(2), 125-133.

Kani, G. (1964). "The riddle of shear failure and its solution." *Proc., Journal Proceedings*, 441-468.

Lee, C., Ko, M., and Lee, Y. (2013). "Bend Strength of Complete Closed-Type Carbon Fiber-Reinforced Polymer Stirrups with Rectangular Section." *Journal of Composites for Construction*, 18(1), 04013022.

Markeset, G., Rostam, S., and Klinghoffer, O. (2006). *Guide for the use of stainless steel reinforcement in concrete structures*, Byggforsk.

Nishizaki, I., Takeda, N., Ishizuka, Y., and Shimomura, T. "A case study of life cycle cost based on a real FRP bridge." *Proc., Third International Conference on FRP Composites in Civil Engineering*, 102.

Nystrom, H. E., Watkins, S. E., Nanni, A., and Murray, S. (2003). "Financial viability of fiber-reinforced polymer (FRP) bridges." *Journal of Management in Engineering*, 19(1), 2-8.

Oden, J. T. (1967). *Mechanics of elastic structures*, New York.

Paglietti, A., and Carta, G. (2009). "Remarks on the Current Theory of Shear Strength of Variable Depth Beams." *The Open Civil Engineering Journal*, 3(1), 28-33.

Razaqpur, A. G., and Spadea, S. (2014). "Shear strength of FRP reinforced concrete members with stirrups." *Journal of Composites for Construction*, 19(1), 04014025.

Schmitt, G. (2009). "Global needs for knowledge dissemination, research, and development in materials deterioration and corrosion control." World Corrosion Organization, 3-8.

Shapira, A., and Bank, L. C. (1997). "Constructability and economics of FRP reinforcement cages for concrete beams." *Journal of Composites for Construction*, 1(3), 82-89.

Spadea, S., Orr, J., and Ivanova, K. (2017). "Bend-strength of novel filament wound shear reinforcement." *Composite Structures*, 176, 244-253.

Spadea, S., Orr, J., Nanni, A., and Yang, Y. (2017). "Wound FRP shear reinforcement for concrete structures." *Journal of Composites for Construction*, 21(5), 04017026.

Stratford, T., and Burgoyne, C. (2003). "Shear analysis of concrete with brittle reinforcement." *Journal of Composites for Construction*, 7(4), 323-330.

Timoshenko, S. (1930). *Strength of materials*, New York.

US Geological Survey (2017). "Mineral Commodity Summaries." USGS, Washington DC, 202.

Vecchio, F. J., and Collins, M. P. (1986). "The modified compression-field theory for reinforced concrete elements subjected to shear." *ACI Journal Proceedings*, 83(2).

Yang, Y., Orr, J., Ibell, T., and Darby, A. "Shear strength theories for beams of variable depth." *Proc., IASS/ISOFF 2015 Annual International Symposium on Future Visions*

599 **Table 1.** Design details of variable-depth beam specimens

Specimen	CFRP flexural bars	d_m (mm)	Shear reinforcement				Expected failure mode
			A_{fv} (mm^2)	s (mm)	α (degrees)	ρ_{fv} (%)	
T1	2 φ 10	195	-	-	-	-	Shear failure
T2-1	2 φ 10	195	8.6	150	40-50	0.25	Shear failure
T2-2	2 φ 10	195	4.3	75	55-67	0.25	Shear failure
T3-1	2 φ 10	195	8.6	75	55-67	0.50	Shear failure
T3-2	2 φ 10	195	4.3	35	71-79	0.50	Shear failure
T4	2 φ 10	195	25.6	150	40-50	0.75	Bending failure
T5-1	2 φ 10	195	4.3	38-60	45	0.45	Shear failure
T5-2	2 φ 10	195	4.3	57-90	45	0.30	Shear failure

600

601

602

603

604

605

606

607

608

609

610

611

612

Table 2. Concrete strength at 28 days

$f_{cm,cube}$ (MPa)	35.8
f_{cm} (MPa)	28.6

Table 3. Corner strength of W-FRP shear links and tensile properties of Aslan bars (Spadea*, et al.*, 2017).

Reinforcement	Cross section area per unit (mm^2)	Ultimate capacity (kN)	Ultimate strength (MPa)	Ultimate strain (%)	Elastic Modulus (GPa)
Transverse W-FRP	4.3	4.1	957	0.89	109
	8.6	6.4	745	0.68	108
	25.7	16.0	623	0.59	105
Longitudinal bar (ø10mm)	71.3	189	2648	1.85	143

Table 4. Summary of test results

Specimen	Ultimate capacity $P_{exp.}$ (kN)	Ultimate shear force $V_{exp.}$ (kN)	Failure mode	Deflection at load point (mm)
T1	32	21	DT	6.9
T2-1	62	41	DT	8.3
T2-2	93	62	SC	14.8
T3-1	95	63	SC	14.1
T3-2	111	74	SC	18.7
T4	100	67	DF	13.2
T5-1	94	63	SC	12.8
T5-2[a]	95	63		11.6
T5-2[b]	89	59	SC	10.3

[a]First test of specimen 5-2; [b]second test of specimen 5-2.

Table 5. Longitudinal bar strains and resulting tensile force

Specimen	T1	T2-1	T2-2	T3-1	T3-2	T4	T5-1	T5-2
Load P (kN)	32	62	93	82	66	88	83	80
Strain ε_f (%)	0.07	0.55	0.77	0.53	0.55	0.99	1.25	1.73
T (kN)	14	113	158	109	113	203	257	355

683 **Table 6.** Strains of shear links crossing the primary shear crack at failure load

Specimen	Cross section area (mm^2)	Strain ε_{fv} (%)					
		Vertical links			Inclined links		
		Minimum	Average[a]	Maximum	Minimum	Average[a]	Maximum
T2-1	8.56	0.44	0.44 (1)	0.44	0.27	0.41 (2)	0.55
T2-2	4.28	0.74	0.87 (2)	1.00	0.43	0.86 (3)	1.07
T3-1	8.56	0.28	0.35 (2)	0.42	0.39	0.48 (3)	0.27
T3-2	4.28	0.81	0.81 (1)	0.81	0.89	0.89 (1)	0.89
T4	25.7	0.14	0.14 (1)	0.14	0.25	0.40 (2)	0.54
T5-1	4.28	0.03	0.47 (6)	0.81	0.37	0.53 (6)	0.78
T5-2	4.28	0.27	0.45 (3)	0.73	0.45	0.63 (4)	0.73

684 Notes: [a]the number of shear links is shown in brackets

685

686

687

688

689

690

691

692

693

694

695

696

697

Table 7. Comparison between the variable-depth beams and prismatic beams

Current research				Previous research (Spadea, *et al.*, 2017)			
Specimen	ρ_{fv} (%)	Q_c (10^{-3} m^3)	$V_{exp.}$ (kN)	Prismatic specimen	ρ_{fv} (%)	Q_c (10^{-3}m^3)	$V_{exp.}$ (kN)
T1	0.00	29.5	21	P1	0.00	36.3	20
T2-1	0.25	29.5	41				
T2-2	0.25	29.5	62	P2	0.31	36.3	60
T5-2	0.30	29.5	63				
T4	0.75	29.5	67	P3	0.84	36.3	74

Table 8. Calibration of codified designs

Specimen	$P_{exp.}$ (kN)	P^*_{ACI} (kN)	P_{ACI} (kN)	$\frac{P_{exp.}}{P^*_{ACI}}$	$\frac{P_{exp.}}{P_{ACI}}$	P^*_{CSA} (kN)	P_{CSA} (kN)	$\frac{P_{exp.}}{P^*_{CSA}}$	$\frac{P_{exp.}}{P_{CSA}}$	P_{MCFT} (kN)	$\frac{P_{exp.}}{P_{MCFT}}$
T1	32	20	11	1.57	2.89	35	19	0.91	1.71	[a]	[a]
T2-1	62	50	31	1.23	2.00	85	51	0.73	1.22	41	1.51
T2-2	93	50	31	1.84	3.00	85	51	1.09	1.82	65	1.42
T3-1	95	80	51	1.18	1.87	124	76	0.77	1.25	94	1.01
T3-2	110	80	51	1.37	2.16	124	76	0.89	1.45	137	0.8
T4	100	110	71	0.91[b]	1.42[b]	156	96	0.64[b]	1.04[b]	126	0.79[b]
T5-1	94	74	47	1.27	2.01	117	71	0.81	1.32	124	0.76
T5-2	95	57	35	1.68	2.73	93	56	1.02	1.68	81	1.18
			Average:	1.45	2.38			0.89	1.49		1.11
			SD:	0.25	0.47			0.13	0.24		0.31

Notes: [a]MCFT cannot give predictions for unreinforced concrete; [b] Results for T4 excluded from average and standard deviation calculations due to premature debonding of this specimen.

Figure

Click here to download Figure Fig.1.tif

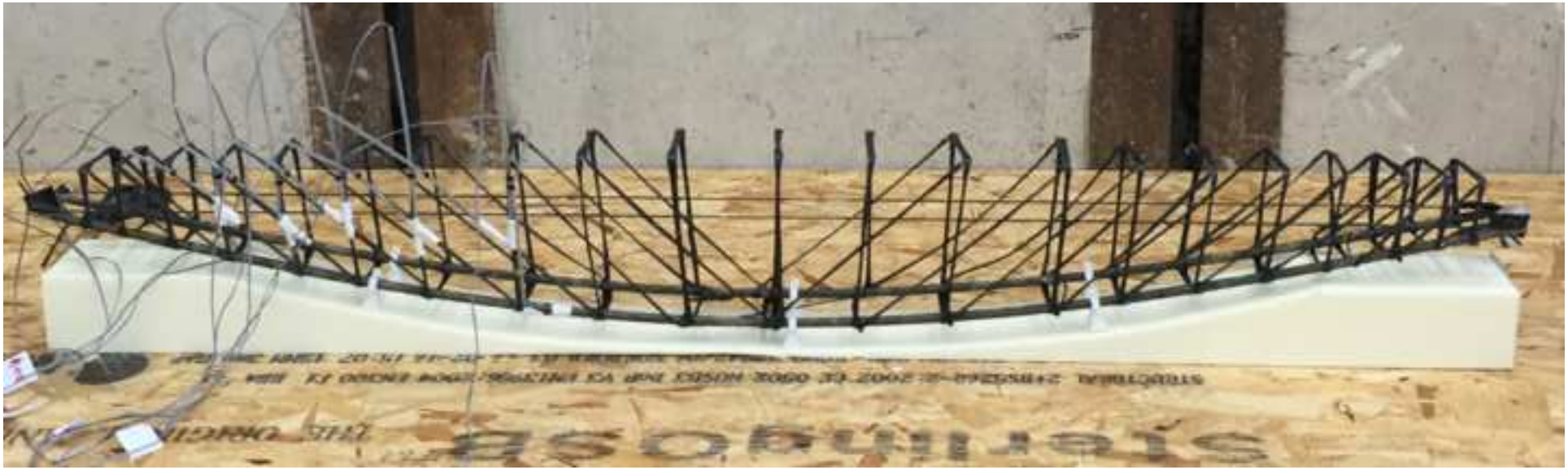

Figure

Click here to download Figure Fig.2.eps

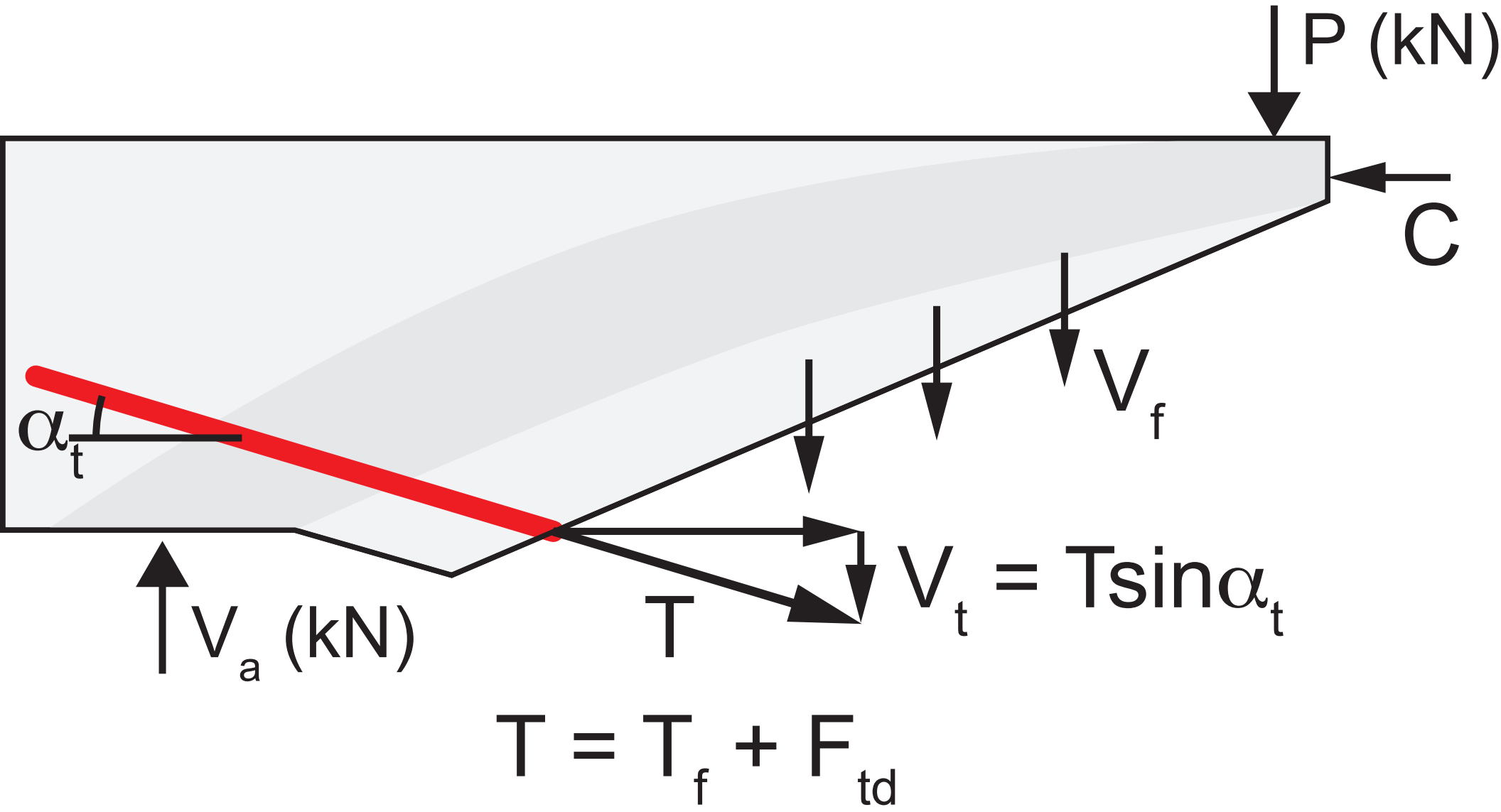

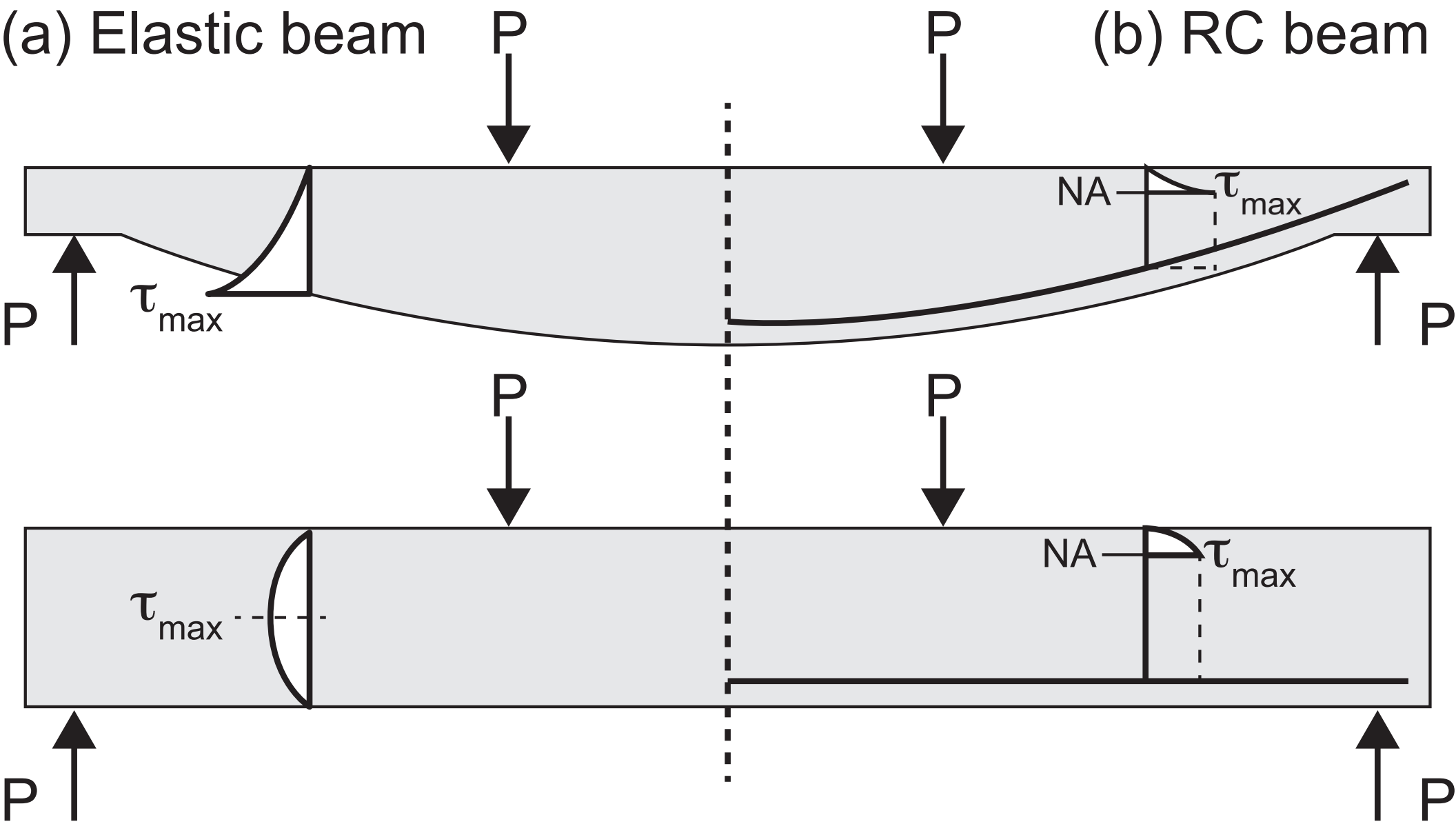

Figure

Click here to download Figure Fig.4.eps

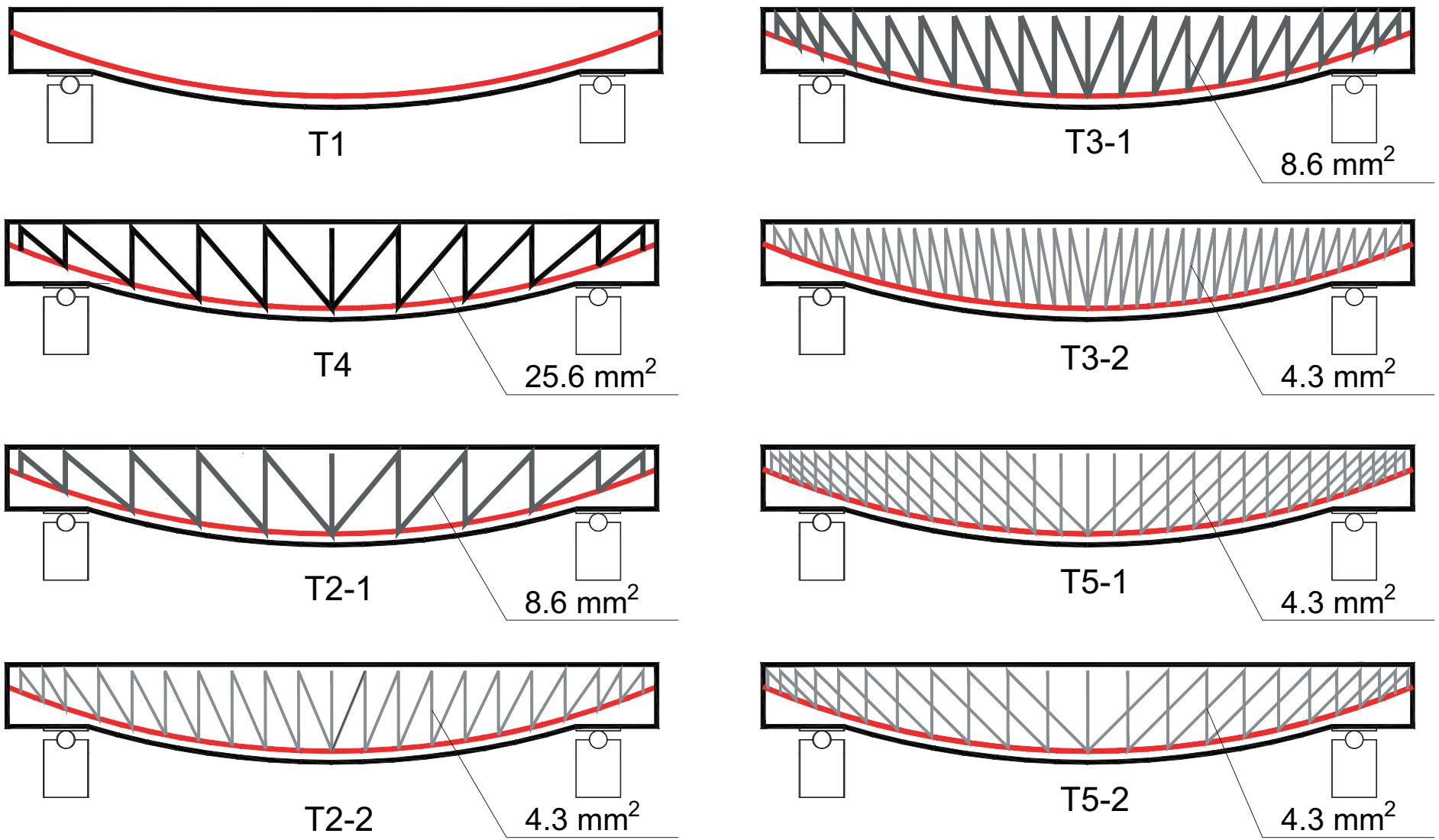

Figure

Click here to download Figure Fig.5.tif

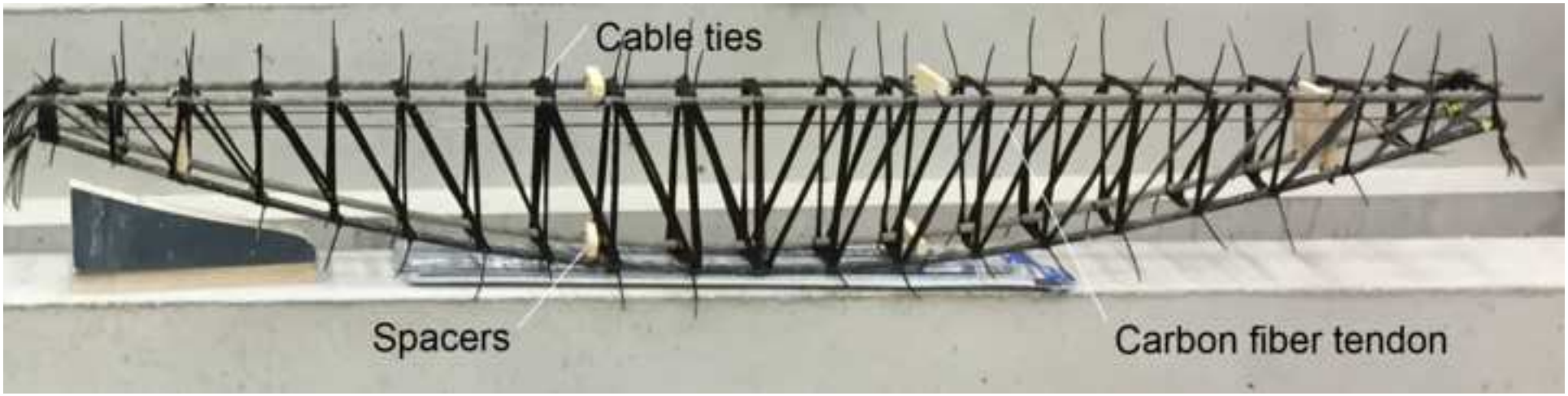

Figure

Click here to download Figure Fig.6.eps

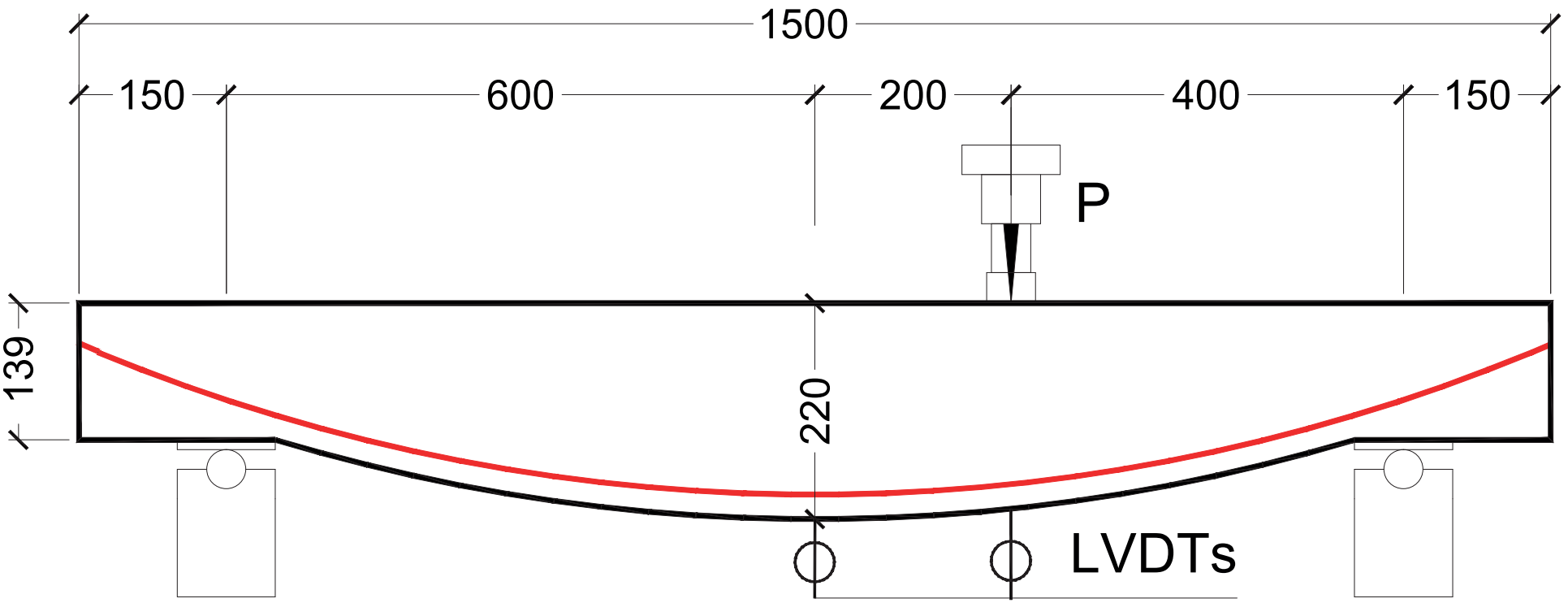

Figure

Click here to download Figure Fig.7.eps

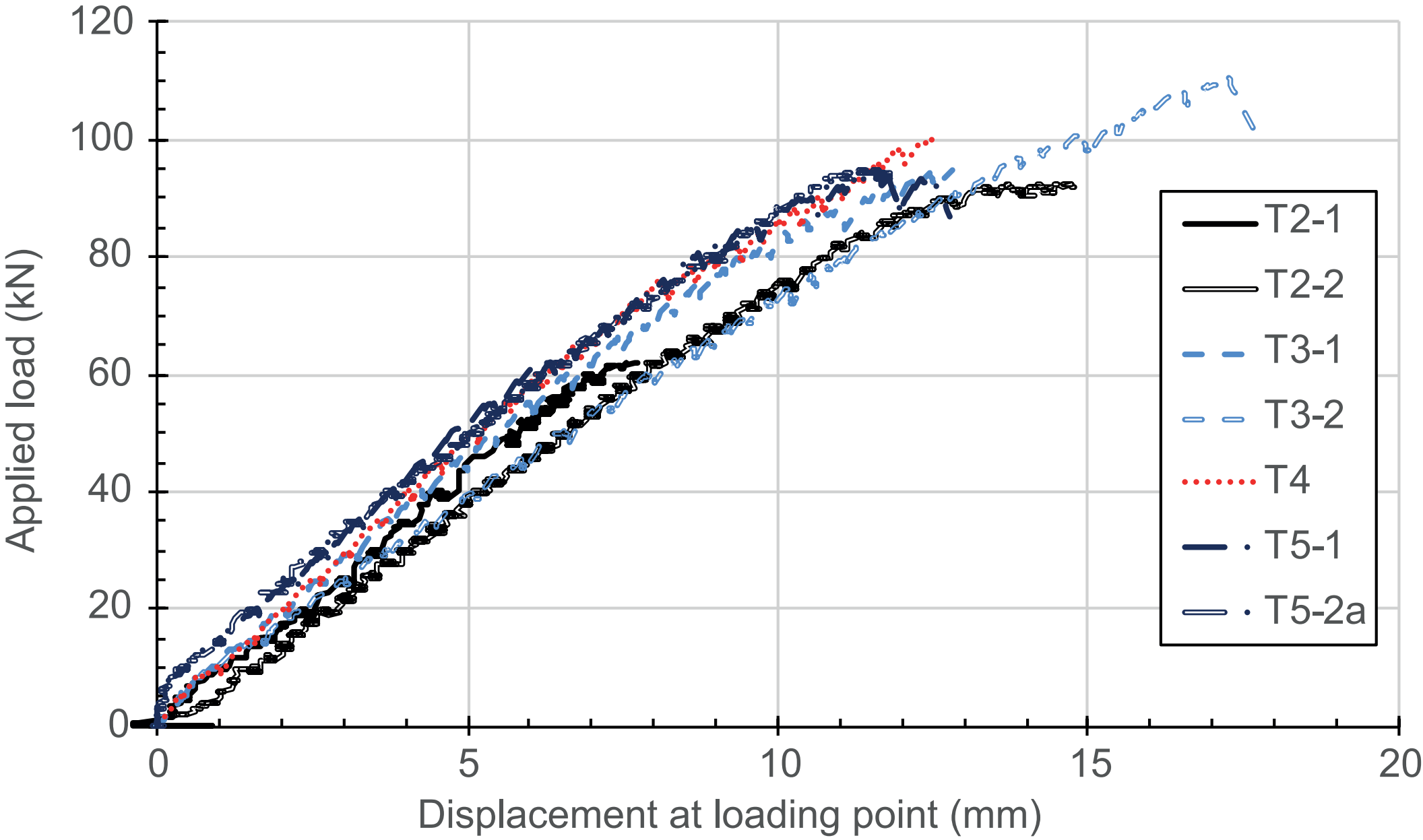

Figure

Click here to download Figure Fig.8.tif

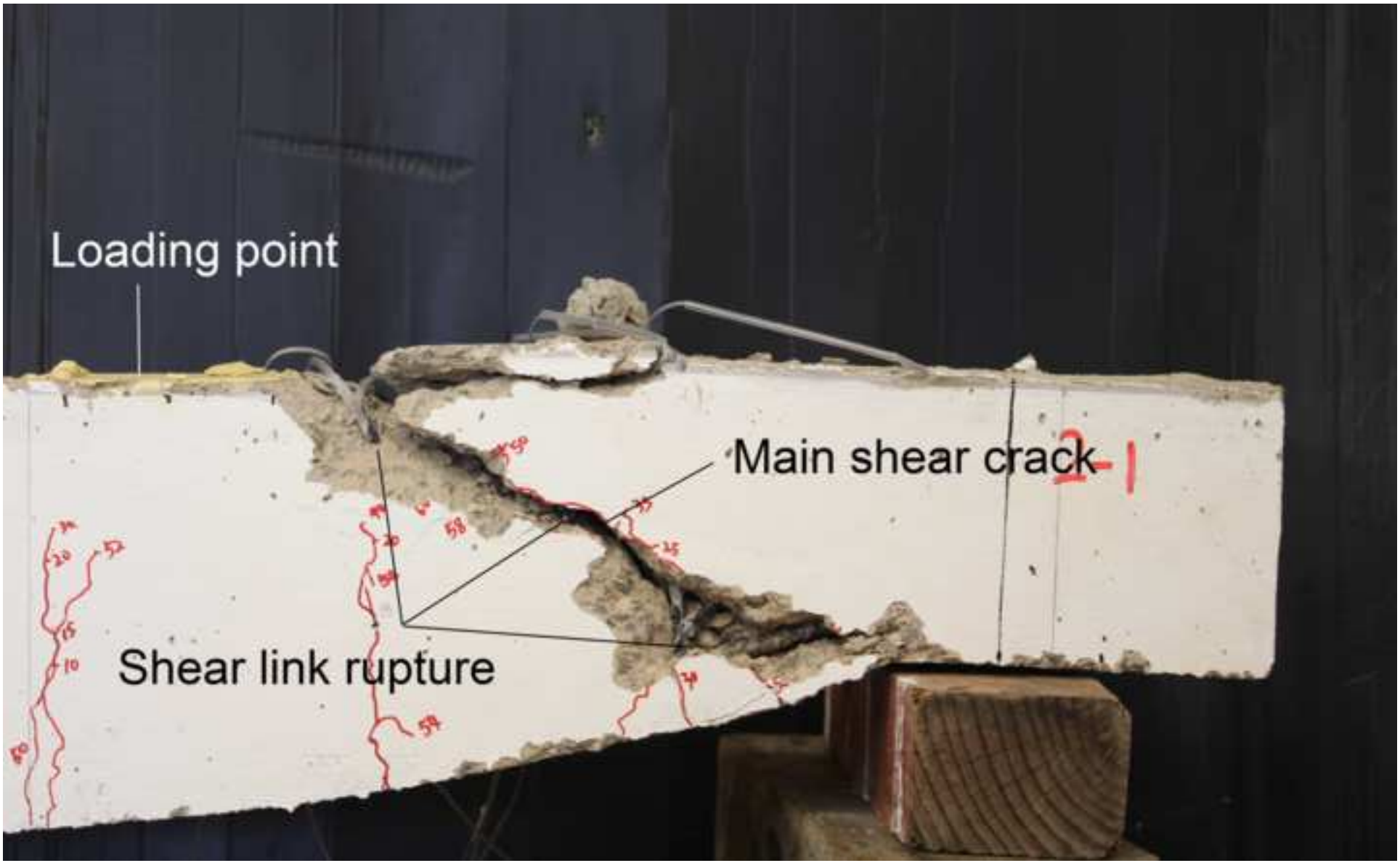

Figure

Click here to download Figure Fig.9.tif

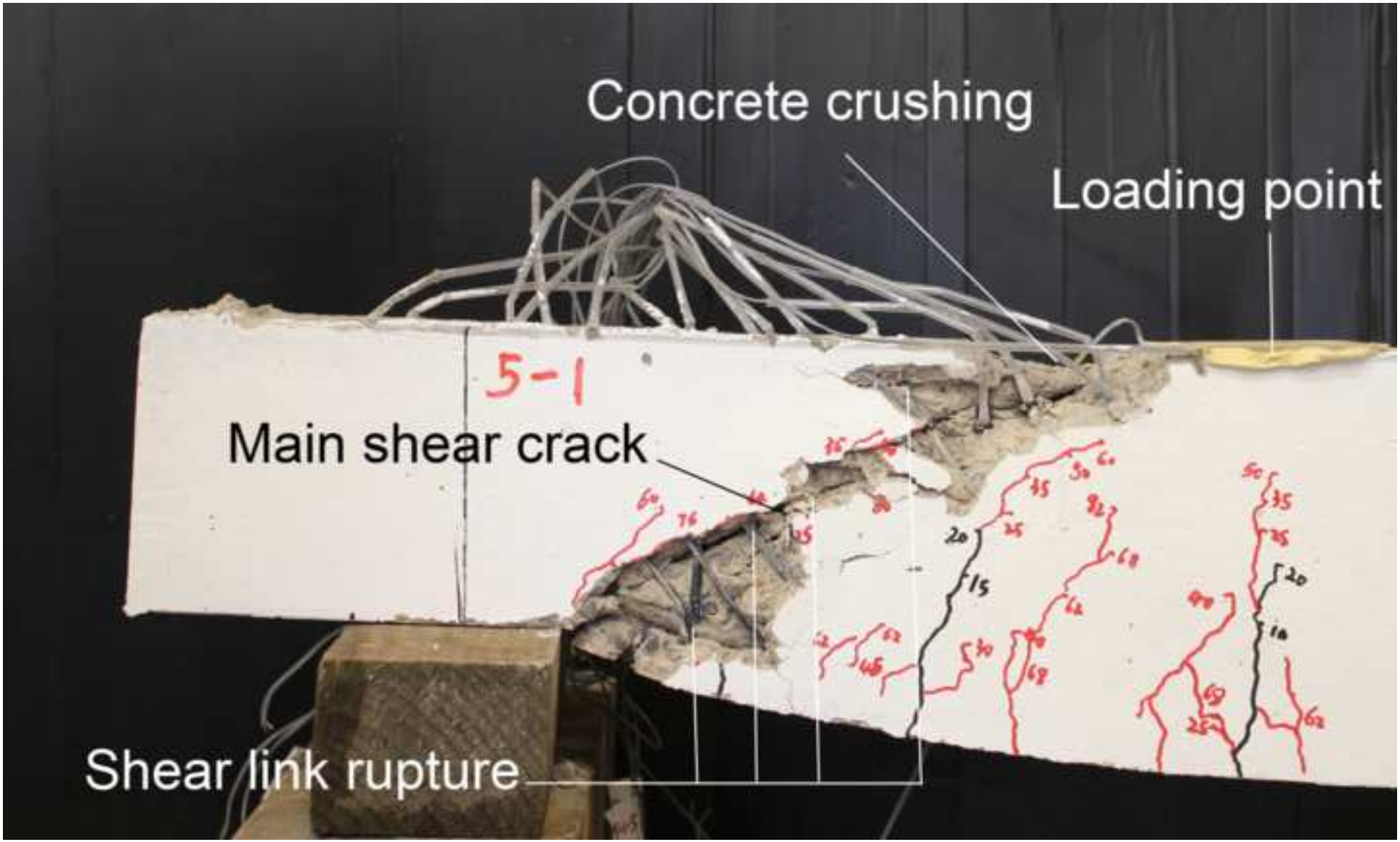

Figure

Click here to download Figure Fig.10.tif

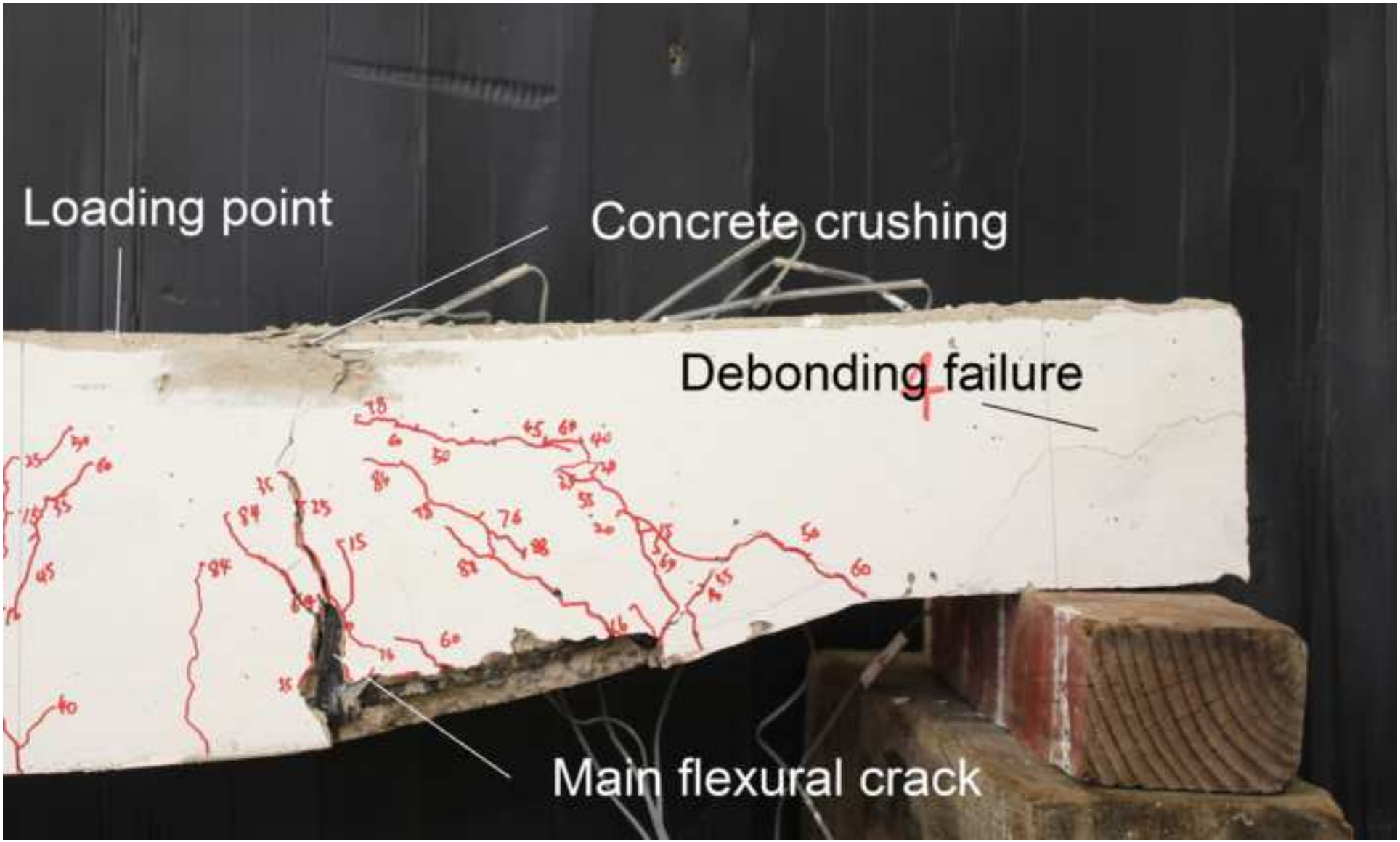

Figure

Click here to download Figure Fig.11.eps

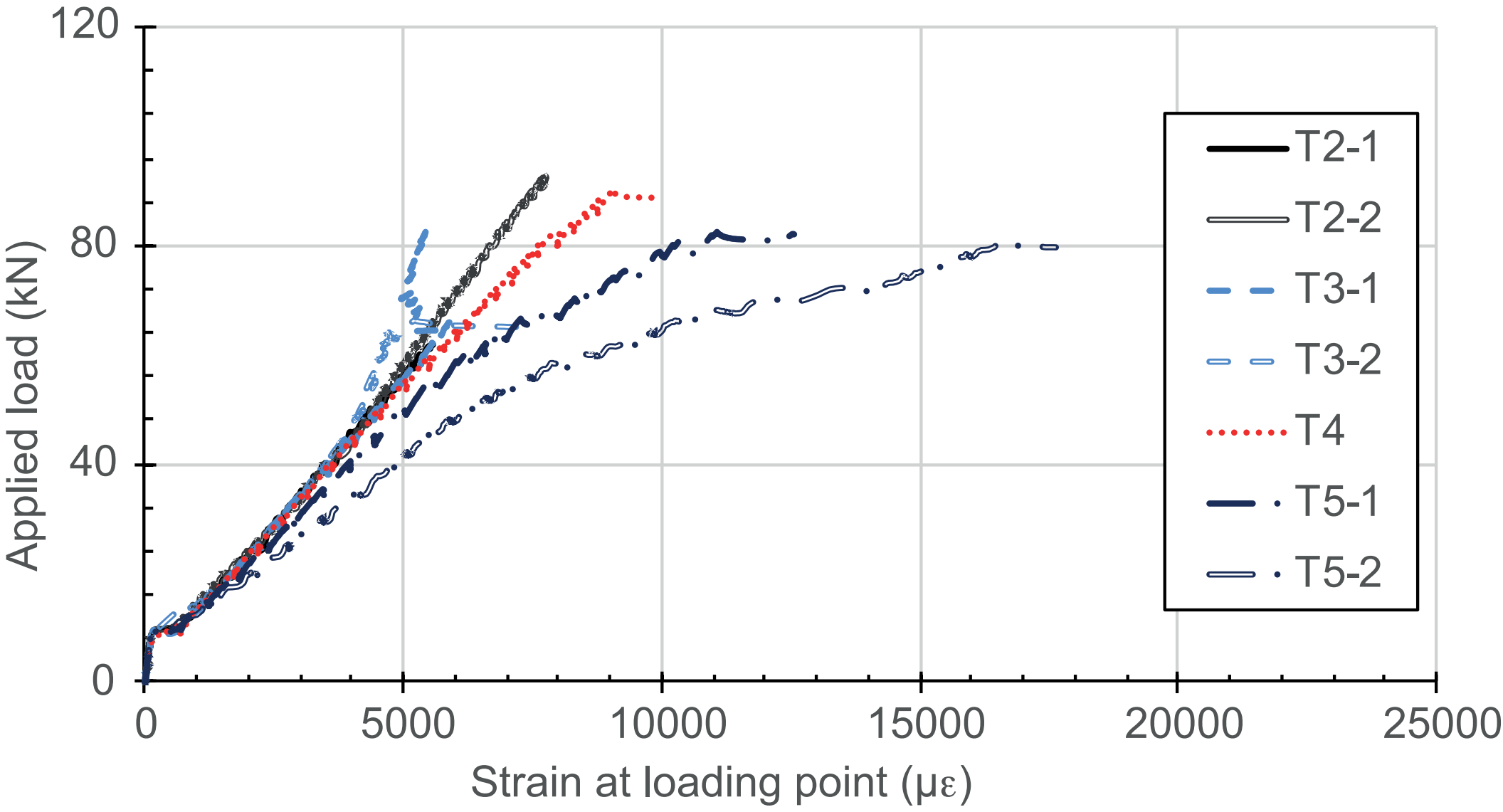

Figure

Click here to download Figure Fig.12.eps

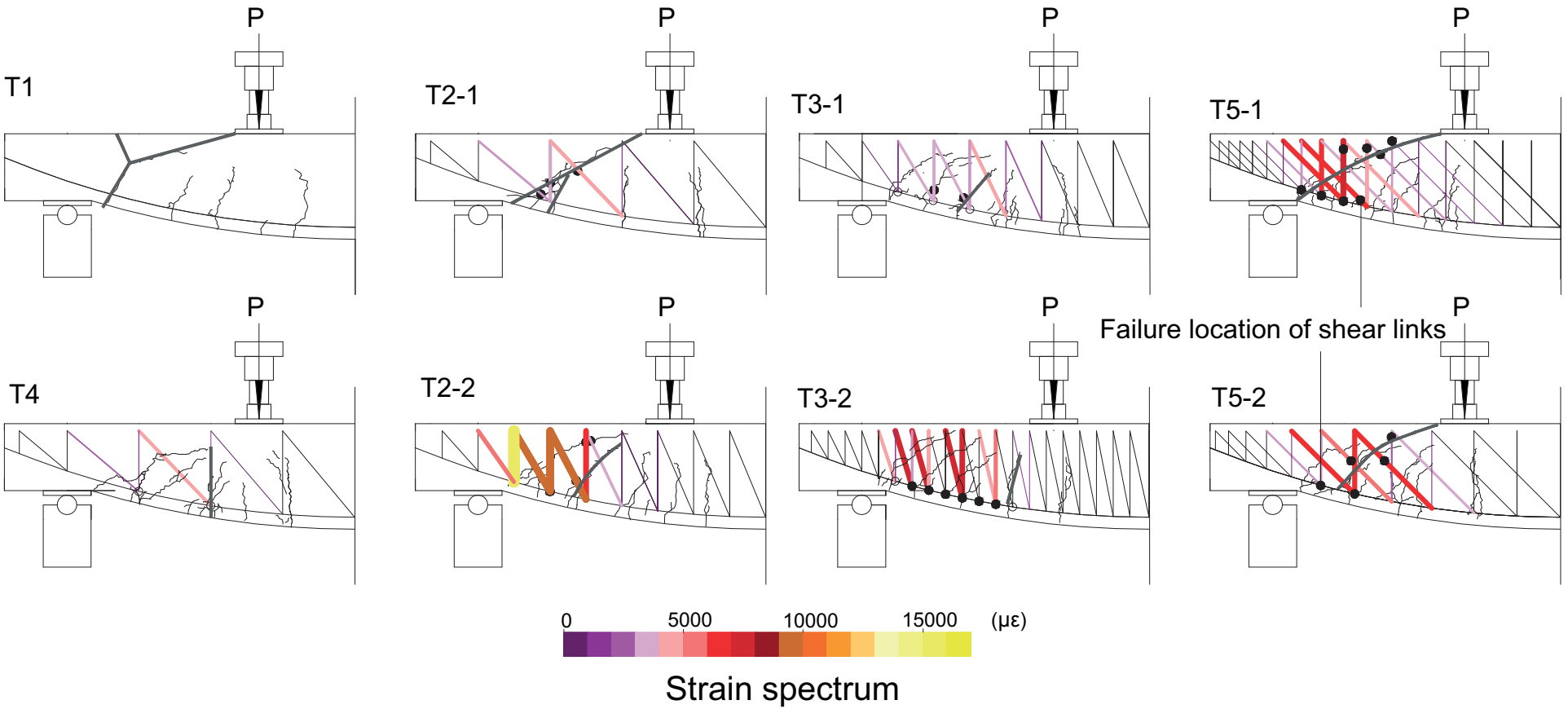

Figure

Click here to download Figure Fig.13.eps